

## **Mechanical and microstructural characterization of new nickel-free low modulus $\beta$ -type titanium wires during thermomechanical treatments.**

**J. Guillem-Martí<sup>1,2,3</sup>, C. Herranz-Díez<sup>1,2</sup>, J. E. Shaffer<sup>4</sup>, F.J.Gil<sup>1,2,3</sup>, J.M. Manero<sup>1,2,3</sup>**

<sup>1</sup> Biomaterials, Biomechanics and Tissue Engineering Group, Department of Materials Science and Metallurgy, Technical University of Catalonia (UPC), ETSEIB, Av. Diagonal 647, 08028 Barcelona, Spain

<sup>2</sup> Biomedical Research Networking Centre in Bioengineering, Biomaterials and Nanomedicine (CIBER-BBN), Campus Río Ebro, Edificio I+D Bloque 5, 1ª planta, C/ Poeta Mariano Esquillor s/n, 50018 Zaragoza, Spain

<sup>3</sup> Centre for Research in NanoEngineering (CRNE) – UPC, C/Pascual i Vila 15, 08028 Barcelona, Spain

<sup>4</sup> Fort Wayne Metals Research Products Corporation, 9609 Ardmore Avenue, 46809 Fort Wayne.

\*Corresponding author:

Dr. J.M. Manero:

Biomaterials, Biomechanics and Tissue Engineering Group, Department of Materials Science and Metallurgy, Technical University of Catalonia (UPC), ETSEIB, Av. Diagonal 647, 08028 Barcelona, Spain.

E-mail address: [jose.maria.manero@upc.edu](mailto:jose.maria.manero@upc.edu)

**Key words:** Nickel-free titanium alloys, pseudo-elasticity, low elastic modulus, wires, large plastic deformation

## **ABSTRACT**

NiTi alloy is the only practical shape memory alloy (SMA) in biomedical use because of its excellent mechanical stability and functionality. However, it is estimated that between 4.5% and 28.5% of the population are hypersensitive to nickel metal, with a higher prevalence in females. Therefore, developing nickel-free low modulus  $\beta$ -type titanium alloys showing shape memory or super elastic behavior would have a great interest in the biomaterials field. Homogeneous 127  $\mu\text{m}$  diameter Ti<sub>25</sub>Hf<sub>21</sub>Nb wires were produced and compared to straight annealed Ti-50.8 at.%Ni (Nitinol) and 90% cold-drawn 316L wires. Microstructural changes taking place during the heat treatment of cold-worked Ti<sub>25</sub>Hf<sub>21</sub>Nb wires were investigated. Large plastic deformation during wire drawing and subsequent annealing led to nano-crystallization and amorphization which may contribute to the observed superelasticity. Mechanical properties were characterized using cyclic uniaxial tension and rotary beam fatigue test modes. A modulus of elasticity of less than 60 GPa and axial recoverable strain of greater than 3% were observed with stress hysteresis resembling a reversible stress-induced martensitic transformation at higher temperatures. The new Ti<sub>25</sub>Hf<sub>21</sub>Nb alloy is an important candidate for developing Ni-free SMAs in the future.

## 1. INTRODUCTION

The increase in average life expectancy, as well as rapid advances in modern surgery require new generations of clinically relevant biomaterials, with enhanced biological and mechanical performance [1]. Shape memory alloys (SMAs) belong to a group of materials known as smart functional materials. One of the commercial uses of SMA exploits its pseudo-elastic properties in the high-temperature (austenitic) phase in isothermal service. Ni–Ti alloy dominates biomedical use because of its excellent corrosion resistance and rather extreme reversible strain limit. These properties combined with good strain-control fatigue resistance, biological and magnetic resonance compatibility, explain the large adoption over the last 20 years, in the production of biomedical devices (catheter guide wires, stents, orthodontic wires, and recent trials in orthopedic use) [2,3].

Unfortunately, concerns have been raised about the composition of nitinol, specifically with the presence of nickel, a potential allergen in select individuals [4,5]. In addition to this, there are concerns over nickel genotoxicity [6], carcinogenicity [7] and potential mutagenicity [8]. Reduction of Ni content or development of Ni-free SMAs is desired by some practitioners to reduce the risks of nickel hypersensitivity and carcinogenicity.

Another aspect frequently reported for load bearing implants is the stress-shielding effect caused by mechanical incompatibility between bone and implant. A material that is significantly stiffer than bone may, dependent upon geometry, hinder bone regeneration and promote fibrous tissue ingrowth [9,10]. To achieve materials that exhibit a low elastic modulus, similar to that of human cortical bone (10-30 GPa) is another challenge for bone substitution in the metal implant field.

Therefore, the possibility of developing Ni-free SMAs or Ni-free low elastic modulus (LEM) alloys has a great interest in the biomaterials field. For these reasons, new  $\beta$ -type titanium alloys showing these properties are also currently being developed [11]. The most common approach consists in using non-toxic  $\beta$ -stabilizing alloying elements, such as Ta, Nb, Mo, Hf and Zr, because the  $\beta$ -phase Ti alloys show lower elastic modulus (LEM) compared to the  $\alpha$ -phase ones [12,13]. Several efforts have been concentrated on the production of natively biocompatible alloys; e.g. the Ti–Nb and the related Ti–Nb–X system (where X = Zr, Ta, Au, O) have yielded alloys with superelastic strains as high as 4.2% without affecting biocompatibility [14-16]. The TiNbHf ternary system has been widely studied by our group and it presents a blend of attractive properties ideal for fabricating orthopedic implants[17,18,27]. For example, by cyclic nanoindentation test, the Ti-16.2Hf-24.8Nb showed a decrease in the apparent elastic modulus up to 42 GPa by increasing the cold work percentage.

On the other hand, nano-grained (NG) materials have attracted increasing interest due to their improved mechanical, as well as, biological properties compared to coarse-grained (CG). In general, NG materials present higher yield strength, better fatigue life, wear resistance and biological behavior than CG materials [19,20]. One of the most efficient methods of fabrication of bulk nanocrystalline materials is the metalworking technology called “severe plastic deformation” (SPD) [20]. For example, cold plastic deformation plays an important role in enhancing the mechanical properties and the functional properties of NiTi SMA [21,22]. A process similar to SPD was recently developed in wire materials through cold working and subsequent annealing to produce ultrafine-grained structures [23], i.e. nano or microcrystalline, which exhibit improved mechanical and functional properties [23-27].

In this research work, homogeneous Ti25Hf21Nb wires were produced at different thermo-mechanical conditions and compared to straight annealed Ti-50.8 at.% Ni (Nitinol) and 90% cold-drawn 316L wires. The nanograin microstructure modification and consequent adjustment of shape and functional properties has been studied.

## **2. EXPERIMENTS AND METHODS**

Bar of the designed alloy was fabricated in an arc melting furnace from CP Ti Gr. 1 bars, Nb foil 99.8% purity and Hf shavings 99.7% by Fort Wayne Metals. Thin 127  $\mu\text{m}$  wires were produced with varying final cold-work cross-sectional reduction of 75%, 95% and 99% followed by constant tension reel-to-reel heat treatment in an argon atmosphere at 650°C. The treatments of cold drawn wire were performed at dwell times of 1s (HT-B) and 3s (HT-A).

The XRD data were collected by a Bruker D8 Advance X-ray diffractometer, with  $\text{CuK}_{\alpha 1}$  radiation, Göbel mirror and SOL-X solid state detector. The diffractograms were obtained from 4° to 120° of 2-theta with a step of 0.02° and a counting time of 9 s. The crystalline phase identification was carried out by using the computer program “EVA” (Produced by Bruker). The software TOPAS (Bruker AXS TOPAS, General profile and structure analysis software for powder diffraction data, V2.0, Bruker AXS, Karlsruhe, Germany, 2000) with the fundamental parameter approach was used for Rietveld refinement [29]. The optimized parameters were background coefficients, zero-shift error, peak shape parameters, scale factor and cell parameters. The values of the pattern dependents,  $R_{\text{wp}}$ , disagreement factor, and statistical reliability factor of Bragg,  $R_B$ , were evaluated and they indicated that fits are satisfactory [29].

TEM micrographs were obtained from radial slabs extracted close to the wire edge using the focused ion beam (FIB) technique. A 1.5 $\mu\text{m}$  thick strip of Pt was deposited at the location of the slab, then trenches on both sides of the strip were milled using a 30

kV/5 nA Ga beam (30 min). Finer milling along both sides of the slab was carried out at 30 kV/0.3 nA until its thickness reached 100nm (**figure 1**). The same beam settings were used to cut the slab loose. In order to check for any radial homogeneity of the microstructure, an additional slab was extracted. Since no significant differences in grain size, morphology and aspect ratio were found, the microstructure was considered homogeneous and only one slab was prepared for each wire.

Both monotonic and cyclic tensile testing was conducted at both 23°C and 150°C at a strain rate of 0.001/s in a 125 mm gage length using an Instron Model 5565 tensile tester with pneumatic grips. Finally, rotary beam fatigue testing at room temperature for Ø 127 µm TiNbHf alloy, NiTi, and cold-drawn 316L were performed.

### **3. RESULTS**

#### **3.1. As received material (bar)**

##### **(i) Chemical analysis**

The composition was verified by quantitative analysis using Energy Dispersive X-ray Spectroscopy (EDS). In **Table I** the values of experimental and theoretical chemical composition for the designed alloy are shown.

##### **(ii) Microstructural studies**

As it is shown in **figure 2**, the as received microstructure consisted of  $\beta$ -equiaxed grains with some martensitic plates inside them. The average  $\beta$ -grain size was  $39.03 \pm 9.2 \mu\text{m}$ .

##### **(iii) TEM studies**

TEM images also demonstrated that this alloy was mainly composed of  $\beta$ -phase equiaxial grains with high dislocation density (figure 3a). In addition,  $\alpha'$ -martensite was observed inside the  $\beta$ -phase grains. It is well known that the presence of  $\omega$  phase

precipitates in  $\beta$  matrix could be confirmed by electron diffraction pattern [30]. In this case omega phase was not observed.

#### (iv) XRD Diffraction studies

The experimental XRD pattern of Ti25Hf21Nb alloy is shown in figure 4. It is found that the microstructure was mainly formed by  $\beta$ -phase with a crystallographic structure of body-centered cubic as well as a minor phase of martensitic  $\alpha''$  with an orthorhombic structure (S.G. Cmcm). The two most intense peaks corresponding to  $\alpha''$  martensitic phase (111 and 002) are partially overlapped by the peak 110 of the  $\beta$  phase. However, the (200) $\alpha''$  peak (third with higher intensity) can be seen clearly confirming its presence. Rietveld refinement yielded a fraction of 61.95 and 38.05 wt.% of  $\beta$  and  $\alpha''$  phases, respectively (weighted profile R factor;  $R_{wp} = 15.5$ ). Rietveld refinement of the experimental peak positions yielded lattice parameters being  $a = 3.3080 \text{ \AA}$  for the  $\beta$  phase (S.G. Im-3m) whereas for the martensitic  $\alpha''$  phase  $a = 3.2507 \text{ \AA}$ ,  $b = 4.9025 \text{ \AA}$  and  $c = 4.6147 \text{ \AA}$  (S.G. Cmcm)

### 3.2. Severely deformed as-drawn microstructure

The as-drawn wire as produced at Fort Wayne Metals medical wire facility had a complex deformed microstructure resulting from the final cold-work. From the SADP reproduced in **Figure 5**, the wire was found to be a mixture of austenite  $\beta$  (BCC), orthorhombic martensite  $\alpha''$  and amorphous phase. The strong crystalline reflections belong to the austenite phase whereas the weak martensite reflections indicate that only a small amount of martensite was retained. A strong diffuse halo may indicate the presence of an amorphous phase. SADP shows arched spots, indicating that the crystal lattice was strained and a preferential orientation is probably inherited from the original grain. SADP results are in agreement with the results of X-ray diffraction.

Lattice distortion is also confirmed in the BF images by the non-uniform contrast visible in the dark regions. In addition to the high density of dislocations, a complex network of twin-like interfaces was observed inside the microstructure (figure 6a). Plastic deformation mechanisms create a high density of interfaces and dislocation networks, which are responsible for the partial amorphization of the crystalline lattice.

The HRTEM images are shown in **figure 6**, exhibiting a microstructure comprising both amorphous and crystalline regions (**figure 6b**). Such microstructure has a great similarity with the microstructures arising from the amorphization of NiTi shape memory alloy under severe plastic deformation based on cold working, such as high pressure torsion (HPT), cold rolling, cold drawing or surface mechanical attrition treatment (SMAT) [24-28].

It is worth noting that microstructures obtained for different final cross-sectional reduction (75%, 95% and 99%) were very similar. Although it is difficult to conclude, it seems that the diffuse halos which indicate the presence of an amorphous phase is lower for less deformed values.

### **3.3. Microstructure of heat-treated wires**

#### **(i) 75 % cold working (75%CW)**

**Figure 7** shows details from the microstructures of wires heat-treated. Comparing these microstructures with the as-drawn microstructure discussed above, it is observed an overall decrease in the lattice strain, segregation of the strained lattice regions and the emergence of a clearly defined nanocrystalline microstructure in both heat treatments. For HT-A wires, the microstructure consisted of uniform submicron regions, with grain size ranging from 220 to 400 nm. Nevertheless, for HT-B wires certain grains showed clearly defined grain boundaries and no internal strain contrast whereas others showed

rather ill-defined boundaries as well as strain contrast. In this case, the grain size ranged from 25 to 90 nm.

Comparing the SADP of the as-drawn microstructure for HT-B wires discussed above (**figure 7b**), the intensity of the halo rings was weaker; suggesting that recrystallization in the amorphous areas has already started. Obviously, lattice strain is reduced compared to the as-drawn sample since the reflections are less arc-shaped.

**(ii) 95 % cold working (95%CW)**

For HT-A wires, most grains showed clearly defined grain boundaries and no internal strain contrast was observed (**figure 8a**). Nanograined regions presented a grain size ranging from 290 to 545 nm ( $\bar{x}$  =387.3 nm). For lower treatments times, coexistence of recrystallized and recovered microstructures was observed together with ill-defined boundaries as well as strain contrast. The recrystallized grains size varied from 50 up to 112 nm ( $\bar{x}$  =103,4 nm). Although in the original alloy omega phase was not present, SADPs from wires showed the existence of  $\omega$  phase with a hexagonal symmetry. When the  $\omega$  transformation is complete, it was found that the orientation relationship between  $\beta$  and  $\omega$  was  $(0001)\omega // (111)\beta; <1120>\omega // <110>\beta$  in agreement with the literature [30]. Furthermore, it was verified that experimental  $\omega$ -lattice parameters  $a_\omega$  could be, approximately, defined as  $\sqrt{2} a_\beta$  and  $c_\omega$  as  $\frac{2}{3} a_\beta$  [33]. The presence of  $\omega$  phase precipitates in  $\beta$  matrix can be confirmed by electron diffraction pattern, as well as, by dark images (**figure 9**).

**(iii) 99 % cold working (99%CW)**

For HT-A wires, microstructure clearly showed defined grain boundaries with a grain size from 342 up to 657 nm ( $\bar{x}$  =454.3 nm); whereas for lower treatments times (HT-B),

the recrystallized grains size were smaller in the range of 50 up to 200 nm ( $\bar{x} = 123.4$  nm)

### 3.4. Mechanical characterization

#### (i) Uniaxial tensile testing

The stress-strain curves obtained for the different materials tested (**Figure 11a**) showed that the elastic modulus of the alloy under study with different grades of cold work (% cw) was similar to that of NiTi and much more lower than the elastic modulus of 316L and Ti6Al4V. **Figure 11b** shows monotonic uniaxial tension true stress-strain data for the 99% cold-worked wire with treatment A. Total strain to rupture was about 6% true strain in both cases with ultimate strength ranging from 800 MPa at elevated temperature to 950 Mpa at room temperature. **Figure 12** shows cyclic uniaxial tension tests that were performed at body temperature (37°C) and at 150°C using an Instron load frame after 99% cw. A modulus of elasticity of less than 60 GPa and axial recoverable strain of greater than 3% were observed with stress hysteresis resembling a reversible stress-induced martensitic transformation at a test temperature of 150°C. Data were compared to straight annealed Ti-50.8 at.%Ni (Nitinol).

#### (ii) The Rotary Beam Fatigue test.

Figure 13 shows the results obtained during the Rotary Beam Fatigue test at room temperature for  $\varnothing$  127  $\mu$ m TiNbHf alloy, NiTi, and typical result for 90% cold-drawn 316L. At room temperature, Ti25Nb21Hf alloy was capable to perform at higher strain values until failure than the other two materials under study.

## 4. DISCUSSION

The microstructure is mainly formed by  $\beta$ -phase with a crystallographic structure of body-centered cubic as well as a second phase of martensitic  $\alpha''$  with an orthorhombic

structure (S.G. Cmcm). The Rietveld refinement yielded a fraction of 38.05% of  $\alpha''$  martensite. It is well known that the shape memory and superelastic effects are based on the formation and reversion of the orthorhombic  $\alpha''$  phase and therefore profound knowledge about the conditions of  $\alpha''$  formation and its stability are crucial. The XRD patterns obtained have a number of similarities with other Ti-Nb [30,31], Ti-Nb-Ta [33] or Ti-Nb-Hf [34] alloys studied in the literature. The literature has shown that the atomic rearrangements of the martensites h.c.p.  $\alpha'$  and orthorhombic  $\alpha''$  depend strongly on the stoichiometry of the parent phase [35, 36]. For example for TiNb systems, higher Nb content results in the formation of  $\alpha''$  in preference to  $\alpha'$ . The transition from hexagonal  $\alpha'$  to orthorhombic  $\alpha''$  martensite was found to lie between 14 and 16.5 wt% Nb. The experimental results are in accordance with the literature since both orthorhombic  $\alpha''$  martensite (figure 2) and a reversible stress-induced  $\alpha''$  martensitic transformation (figure 12) have been observed for the new Ti<sub>24</sub>Nb<sub>21</sub>Hf alloy.

Moreover, the presence of  $\omega$  phase precipitates in  $\beta$  matrix can be confirmed by electron diffraction pattern as well as by dark images (**figure 9**). A deformation-induced  $\omega$ -phase transformation is expected to occur during cold-working processes because there was no  $\omega$  phase in the original alloy (figure 3). In agreement with the present results, it is reported that high applied strain might induce the  $\omega$ -phase. In the case of Ti and their alloys, it has been reported that high applied strain might induce the  $\omega$ -phase [37, 38]. For TiNb alloys and depending on the concentration of  $\beta$ -stabilizing elements, severe deformation by wire drawing may yield martensite to  $\omega$ -phase formation or  $\beta$  to  $\omega$  transformation at relatively low strain [39].

For the new Ti<sub>25</sub>Nb<sub>21</sub>Hf alloy, the thermal stability of the  $\omega$ -phase has been found to be considerably larger than that of  $\omega$ -Ti (140°C) and  $\omega$ -Zr (250°C) [40]. However, after

the applied heat treatments (650°C at 1s and 3s),  $\omega$  phase is still remaining. Further studies will be necessary in order to promote the  $\omega$  to  $\beta$  transformation in terms of anneal treatments parameters.

Thin wires produced with cold-work cross-sectional reduction and subsequent thermal treatment can strongly enhance mechanical properties; especially, in terms of mechanical strength and cyclic fatigue behavior due to grain refinement down to the submicron scale (figures 11-14). Furthermore, the elastic modulus value of the nano-grained Ti<sub>24</sub>Nb<sub>21</sub>Hf alloy was 30 to 40% lower than those of its coarse-grained counterpart. Original alloy (size grain, 39  $\mu\text{m} \pm 9.2$ ) has a value of 86 GPa while, in all the cases, the modulus obtained for the nano-grains wires were between 50 GPa and 59 GPa (Figure 11). Indeed, lower values are obtained for microstructures having a smaller grain size, that is, wires treated at 650°C for 1 second (HT-B).

There are some reports showing a reduction in the elastic moduli of some nanocrystalline materials, compared with the corresponding coarse-sized crystalline materials [41-43]. Due to the extremely small dimensions of grains, a large volume fraction (e.g. up to 40%) of atoms reside in interface regions. It is reported that the large volume fraction of distorted atomic structure could induce the reduction of the elastic modulus. Furthermore, the formation of ultrafine-grained structures with high-angle and non-equilibrium grain boundaries capable of grain-boundary sliding (GBS) increases ductility [43].

The 99% cold work sample with treatment A, exhibited reversible strain up to about 4% true strain when tested at 150°C. Unlike pseudoelasticity in typical binary Ti-Ni (see Figure 12), the transformation region displayed some hardening slope as opposed to a flat plateau. This effect is attributed to deformation mechanisms changing as a function of temperature. At room temperature (see Figure 11b), the treated Ti<sub>25</sub>Hf<sub>21</sub>Nb wire,

exhibited the typical flat loading plateau associated with low stress martensite detwinning and Luders-like deformation. At elevated temperature ( $>A_f$ ) it is likely that distinct stress-induced variants were selected during deformation and that the near-yield stresses generated some plastic flow and hardening during partial transformation.

Finally, it is shown that thin wires present a considerable increase in fatigue life in comparison with a similar 90% cold-drawn 316L or superelastic Nitinol wires ( $A_f > 15^\circ\text{C}$ ). This is very important because the Ti25Nb21Hf alloy was capable of performing at higher strain values until failure than the other two alloys. In terms of nanomaterials processing, a noticeable increase in both low and high cycle fatigue has been reported [44,45]. For example, it was shown that fine grained Cp Ti Gr.1 processed by ECAP (equal-channel angular pressing) revealed a considerable increase in fatigue life and fatigue limit when compared with those in the coarse-grain state [46].

Regardless of the wires, for orthopedic applications the low Young's modulus close to that of human bone is helpful to minimize the stress shielding effect [47]. Most commercial alloys used as implant materials present an elastic modulus in the range of 110 GPa for Ti6Al4V up to 220 GPa for cobalt-chrome alloys. It has been demonstrated that, by means of thermo-mechanical treatments (severe plastic deformation), the mechanical properties have been enhanced by lowering young's modulus up to 50 GPa. Although still higher than the Young's modulus of cortical (dense) bone, this alloy is a candidate for load bearing implant applications by preliminary fatigue and stiffness characteristics. It is well known that the Young's modulus of the alloy is related to the different Young's modulus values of the different phases present in the microstructure [47]. In general,  $E_\beta < E_{\alpha''} < E_{\alpha'} < E_\omega$ , therefore it could be interesting to carry out further studies in order to remove the  $\omega$ -metastable phase; as for example by modifying the heat-treatments parameters. Therefore, properties such as high strength, low elastic

modulus, potential pseudo-elasticity and good biocompatibility may provide value in many applications.

## **5. CONCLUSIONS**

A new nickel-free low modulus  $\beta$ -type titanium alloy showing superelastic behavior has been characterized. A modulus of elasticity of less than 60 GPa and axial recoverable strain of greater than 3% were observed with stress hysteresis resembling a reversible stress-induced martensitic transformation at higher temperatures. The ability of  $\beta$ -TiNbHf alloy to undergo cold deformation with high reductions is of great importance. For one, this aspect enables readily scalable process conditions and because high deformation (with up to 99% reduction in cross section) combined with subsequent recrystallization upon continuous rapid heating allows formation of submicron-grained microstructure, with an excellent balance of good recoverability, high strength, acceptable ductility and fatigue strength. The microstructural modification and consequent adjustment of shape and functional properties by means of thermomechanical treatment is effective in enhancing its mechanical properties. Homogeneous Ti<sub>25</sub>Hf<sub>21</sub>Nb wires compared to straight annealed Ti-50.8 at.%Ni (Nitinol) and 90% cold-drawn 316L wires showed attractive properties in terms of low elastic modulus and rotary beam fatigue behavior. Nevertheless, further studies will aid in further body-temperature, superelastic, property improvements. In summary, the low cytotoxicity and excellent hemocompatibility, as well as its mechanical properties make it as an important nickel-free SMA candidate.

## **5. REFERENCES**

[1] Leon Mishnaevsky Jr et al. Nanostructured titanium-based materials for medical implants: Modeling and development. *Materials Science and Engineering R* 81 (2014) 1–19.

- [2] Lorenza Petrini, Francesco Migliavacca. Biomedical Applications of Shape Memory Alloys. *Journal of Metallurgy*. Volume 2011 (2011), Article ID 501483, 15 pages.
- [3] M.Roshdi Hassan, Y.T Haw. Shape memory alloys applications in bone fixation: State of the art. *Applied Mechanics and Materials*. Vol 680. (2014). Pp 119-122.
- [4]. Lu XY, Bao X, Huang Y, Qu YH, Lu HQ, Lu ZH. Mechanisms of cytotoxicity of nickel ions based on gene expression profiles. *Biomaterials* 2009, 30, 141–148
- [5] M.Berger-Gorbet, B.Broxup, C.Rivard, L.H. Yahia. Biocompatibility testing of Ni–Ti screw using immuno histochemistry on sections containing metallic implants. *J Biomed Mater Res*, 32 (1996), pp. 243–248
- [6] Assad M, Lemieux N, Rivard C, Yahia L. Comparative in vitro biocompatibility of nickel-titanium, pure nickel, pure titanium, and stainless steel: genotoxicity and atomic absorption evaluation. *Bio-Med Mater Eng* 1999;9:1–12.
- [7] Beyersmann D, Hartwig A. Carcinogenic metal compounds: recent insight into molecular and cellular mechanisms. *Arch Toxicol* 2008;82(8):493–512.
- [8] Yamamoto A, Kohyama Y, Hanawa T. Mutagenicity evaluation of forty-one metal salts by the umu test. *J Biomed Mater Res* 2002;59(1):176–83.
- [9] D.R. Sumner, T.M. Turner, R. Igloria, R. Urban, J.O. Galante. Functional adaptation and ingrowth of bone vary as a function of hip implant stiffness. *J Biomech*, 31 (1998), pp. 909–917
- [10] M. Geetha, A.K. Singh, R. Asokamani, A.K. Gogia. Ti based biomaterials, the ultimate choice for orthopaedic implants – A review. *Progress in Materials Science* 54 (2009) 397–425
- [11] M. Niinomi, M. Nakai, J. Hieda. Review: Development of new metallic alloys for biomedical applications. *Acta Biomaterialia* 8 (2012) 3888–3903
- [12] H.Y. Kim, Y. Ohmatsu, J.I. Kim, H. Hosoda, and S. Miyazaki. Mechanical properties and shape memory behaviour of Ti-Nb alloys. *Mater. Trans.*, 2004, vol. 45, pp. 1090–95.
- [13] T. Ozaki, H. Matsumoto, S. Watanabe, and S. Hanada. Beta TiNbSn alloys with low young's modulus and high strength. *Mater. Trans.*, 2004, vol. 45, pp. 2776–79.
- [14] Miyazaki S, Kim HY, Hosoda H. Development and characterization of Ni-free Ti-base shape memory and superelastic alloys. *Mater Sci Eng, A* 2006;438–440:18–24.
- [15] Hosoda H, Fukui Y, Inamura T, Wakashima K, Miyazaki S, Inoue K. Mechanical properties of Ti-based shape memory alloys. *Mater Sci Forum* 2003;426–432:3121–6.

- [16] Kim HY, Ikehara Y, Kim JI, Hosoda H, Miyazaki S. Martensitic transformation, shape memory effect and superelasticity of Ti–Nb binary alloys. *Acta Mater* 2006;54:2419–29.
- [17] M. González, J.M. Manero, M. Arciniegas, and F.J. Gil. Optimization of the Ti-16.2Hf-24.8Nb-1Zr Alloy by Cold Working. *J. Materials Eng. and Performance*. Vol 18(5) 2009. 506-10.
- [18] M. González, J. Peña, F.J. Gil, J.M. Manero. Low modulus Ti-Nb-Hf alloy for biomedical applications. *Materials Science & Engineering C*. Vol.42, 1 September 2014, Pages 691–695.
- [21] M. Ramalingam, A.Tiwari, S. Ramakrishna, H.Kobayashi. *Integrated Biomaterials for Biomedical Technology: Chapter 6: New kind of titanium alloys for biomedical applications*. John Wiley & Sons. 2012.
- [22] J. Frenzel, E.P. George, A. Dlouhy, C. Somsen, G. Eggeler. Influence of Ni on martensitic phase transformations in NiTi shape memory alloys. *Acta Mater*. 58 (2010) 3444–3458.
- [23] J.E. Schaffer. Fatigue damage resistant wire and method of production thereof. (pat) US 8840735 B2. U.S. Patent and Trademark Office. Sep 23, 2014.
- [24] S. Jiang, L. Hu, Y. Zhang, Y. Liang. Nanocrystallization and amorphization of NiTi shape memory alloy under severe plastic deformation based on local canning compression. *J. of Non-Crystalline Solids* 367 (2013) 23–29.
- [25] Y Zhang, S Jiang, L Hu, Y Liang Deformation mechanism of NiTi shape memory alloy subjected to severe plastic deformation at low temperature. *Materials Science and Engineering: A* Vol 559, 2013, Pages 607–614.
- [26] Shuyong Jiang, Li Hu, Yanan Zhao, Yanqiu Zhang, Yulong Liang. Multiscale investigation of inhomogeneous plastic deformation of NiTi shape memory alloy based on local canning compression. *Materials Science & Engineering A* 569 (2013) 117–123
- [27] Jeremy E. Schaffer. Structure-Property Relationships in Conventional and Nanocrystalline NiTi Intermetallic Alloy Wire. *J. Mat. Eng. and Performance*. (2009). 584 Vol. 18(5–6) 2009
- [28] M. González, E. Salvagni, J.C. Rodríguez-Cabello, E. Rupérez, F.J. Gil, J.M. Manero. A low elastic modulus Ti-Nb-Hf alloy bioactivated with an elastin-like protein-based polymer enhances osteoblast cell adhesion and spreading. *J Biomed Mater Res Part A* 2013;101,819–26.
- [29] R. A. Young, *The Rietveld Method*. Oxford University Press, Oxford, 1993

- [30] D. De Fontaine and O. Buck. A Monte Carlo simulation of the omega phase transformation. *Philos. Mag.* Vol 27, 1973 p697.
- [31] Hon, Y. H. & Wang Y.N, J. Y. and P. Composition/Phase Structure and Properties of Titanium-Niobium Alloys. *Mater. Trans.* 44, 2384 (2003).
- [32] H.Y. Kim, Y. Ikehara, J.I. Kim, S. Miyazaki. Martensitic transformation, shape memory effect and superelasticity of Ti–Nb binary alloys. *Acta Materialia* 54 (2006) 2419–2429.
- [33] Zhou, Y.L, M. Akahori, T. Changes in mechanical properties of Ti alloys in relation to alloying additions of Ta and Hf. 14th Int. Conf. Strength Mater. 483-84, 153–156 (2008).
- [34] Hon, Y. H., Wang, J. Y. & Pan, Y. N. Influence of hafnium content on mechanical behaviors of Ti–40Nb–xHf alloys. *Mater. Lett.* 58, 3182–3186. (2004).
- [35] M. Bönisch, M. Calin, L. Giebeler, W. Skrotzki, J. Eckert. Composition-dependent magnitude of atomic shuffles in Ti-Nb martensites, *J. Appl. Cryst.* 47 (2014) 1374–1379.
- [36] M. Bönisch, M. Calin, T. Waitz, A. Panigrahi, J.Eckert, Thermal stability and phase transformations of martensitic Ti–Nb alloys, *Sci. Technol. Adv. Mater.* 14 (2013). 055004.
- [37] Y. Ivanisenko, A. Kilmametov, H. Rösner, R.Z. Valiev, Evidence of  $\alpha \rightarrow \omega$  phase transition in titanium after high pressure torsion, *Int. J. Mat. Res.* 99 (2008) 36–41.
- [38] P.S. Ghosh, A. Arya, R. Tewari, G.K. Dey, Alpha to omega martensitic phase transformation pathways in pure Zr, *J. Alloys Comp.* 586 (2014) 693–698.
- [39] Y.B. Wang, Y.H. Zhao, Q. Lian, S.P. Ringer, Y.T. Zhu, E.J. Lavernia, Grain size and reversible beta to omega phase transformation in a Ti alloy, *Scripta Mater.* 63 (2010) 613–616.
- [40] K. Edalati, Z. Horita, S. Yagi, E. Matsubara, Allotropic phase transformation of pure zirconium by high-pressure torsion, *Mater. Sci. Eng. A523* (2009) 277–281
- [41] G.F. Wang, X.Q. Feng, S.W. Yu, C.W. Nan. Interface effects on effective elastic moduli of nanocrystalline materials. *Materials Science and Engineering A363* (2003) 1–8
- [42] M. González, F.J. Peña, F.J. Gil, J.M. Manero. “Influence of cold work in the elastic modulus of the Ti-16.2Hf-24.8Nb-1Zr alloy characterized by instrumented nanoindentation”. *Key engineering materials.* (2010) 423, pp. 113 – 118
- [43] Ruslan Valiev. Nanostructuring of metals by severe plastic deformation for advances properties. *Nature Materials.* Vol 3. August 2004. 511-16

- [44] M.A. Meyers , A. Mishra, D.J. Benson. Mechanical properties of nanocrystalline materials  
Progress in Materials Science 51 (2006) 427–556
- [45] Y. Estrin a,A. Vinogradov. Extreme grain refinement by severe plastic deformation: A  
wealth of challenging science. Acta Materialia 61 (2013) 782–817
- [46] Vinogradov AY, Stolyarov VV, Hashimoto S, Valiev RZ. Cyclic behavior of ultrafine-  
grain titanium produced by severe plastic deformation. Mater Sci Eng A 2001;318:163–73.
- [47] Y. Noyama<sup>1</sup>, T. Miura<sup>1</sup>, T. Ishimoto, T. Itaya, M. Niinomi and T. Nakano. Bone Loss and  
Reduced Bone Quality of the Human Femur after Total Hip Arthroplasty under Stress-Shielding  
Effects by Titanium-Based Implant. Materials Transactions, Vol. 53, No. 3 (2012) pp. 565-70
- [48] H.S. Kim, On the rule of mixtures for the hardness of particle reinforced composites,  
Mater. Sci. Eng. A289 (2000) 30–33.

## LEGENDS

**Figure 1** Slabs extracted close to the wire edge using the focused ion beam (FIB) technique.

**Figure 2** Optical micrograph showing  $\beta$  grains with some martensitic plates inside.

**Figure 3.** a)  $\beta$ - phase equiaxed grains with a high dislocation density (zone axis [013]) .b)  $\alpha''$ - martensitic plates inside the  $\beta$  grains.

**Figure 4.** X Ray Diffraction pattern showing mainly  $\beta$  phase (PDF 00-044-1288  $\beta$ -Ti; S.G. Im-3m (229); PDF 01-071-9958 Nb<sub>0.3</sub>Ti<sub>0.7</sub>; S.G orthorhombic Cmc<sub>2</sub>m(63).

**Figure 5.** Microstructure of wire deformed at different magnifications (12K, 25K and 75K) corresponding to scale bar 500, 200 and 100nm respectively. a) As-drawn 75%, b) 95% As-drawn.

**Figure 6.** TEM photographs of alloy subjected to deformation by 95%; a) TEM bright field image showing a complex network of twin-like interfaces and non- uniform contrast visible regions; b) HRTEM image, corresponding to the area marked with a circle, showing the presence of nanocrystalline phase and amorphous phase.

**Figure 7.** 75 % CW microstructures at different magnifications. Scale bar 500, 200 and 100nm respectively. The upper file corresponds to HT-A treatment whereas at the bottom HT-B treatment

**Figure 8.** 95 % CW microstructures at different magnifications

**Figure 9.** Bright and dark field micrographs showing  $\omega$  phase.

**Figure 10.** 99 % cold working microstructures at different magnifications. Scale bar 500, 200 and 100nm, respectively

**Figure 11 a).** Uniaxial tensile testing data for Ti-Hf-Nb alloy tested at room temperature ( $T = 25^\circ\text{C}$ ) at a strain rate of  $10^{-3} \text{ s}^{-1}$ . b) Monotonic uniaxial tension true stress-strain data for the 99% cold-worked wire with treatment A

**Figure 12** Comparison of the uniaxial tensile behavior of the alloy TiNbHf ( $T = 150^\circ\text{C}$ ) and Ti-50.8 at.% Ni ( $T= 25^\circ\text{C}$ ).

**Figure 13.** Results obtained during the Rotary Beam Fatigue test at room temperature for  $\emptyset$  127  $\mu\text{m}$  TiNbHf alloy  $A_f > 100$ , NiTi  $A_f > 15$  and typical result for 90% cold-drawn 316L.

Figure 1

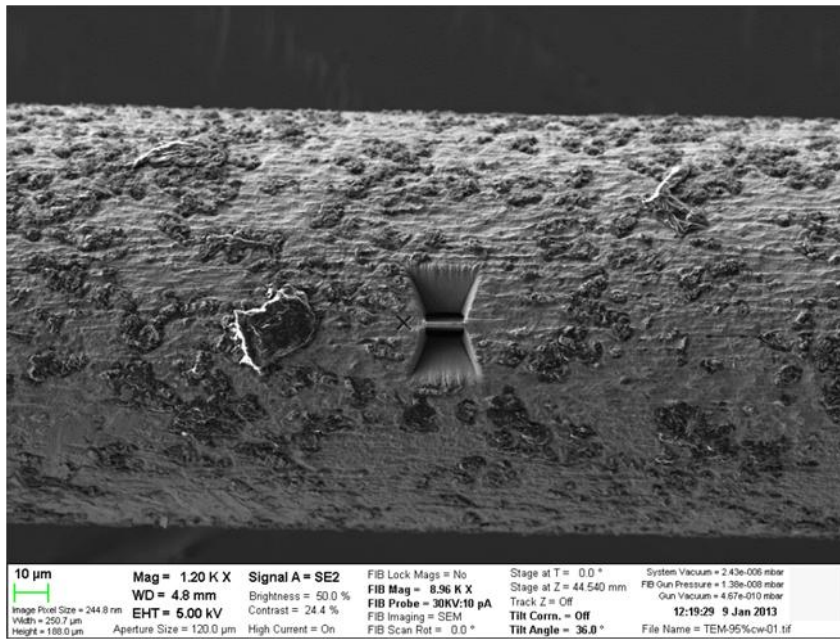


Figure 2

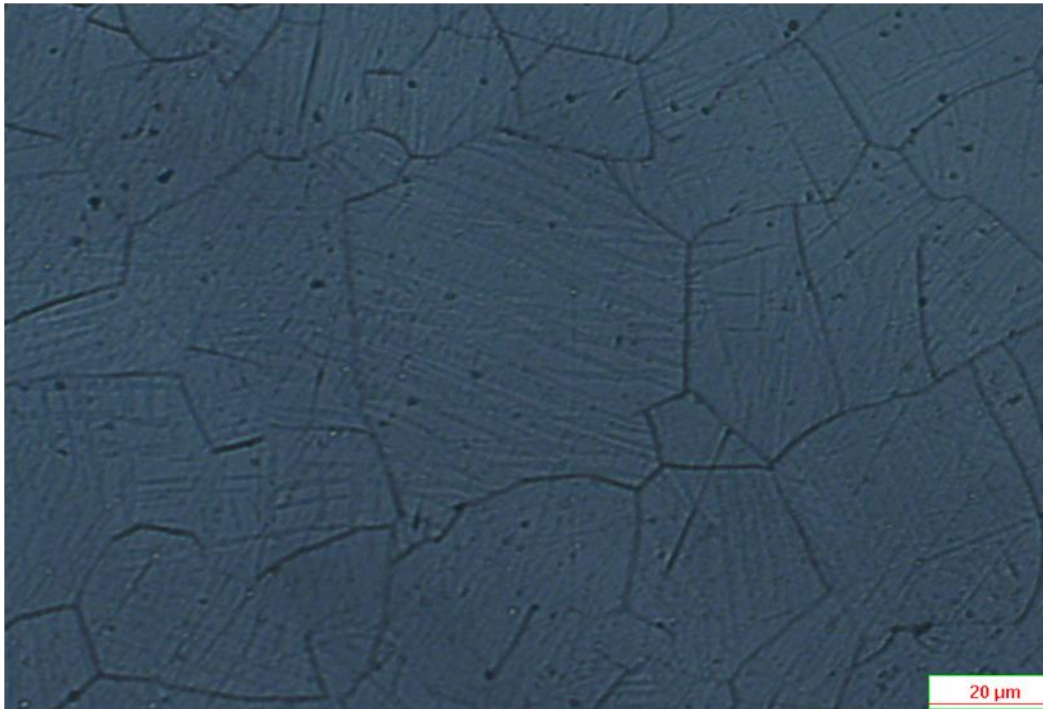


Figure 3

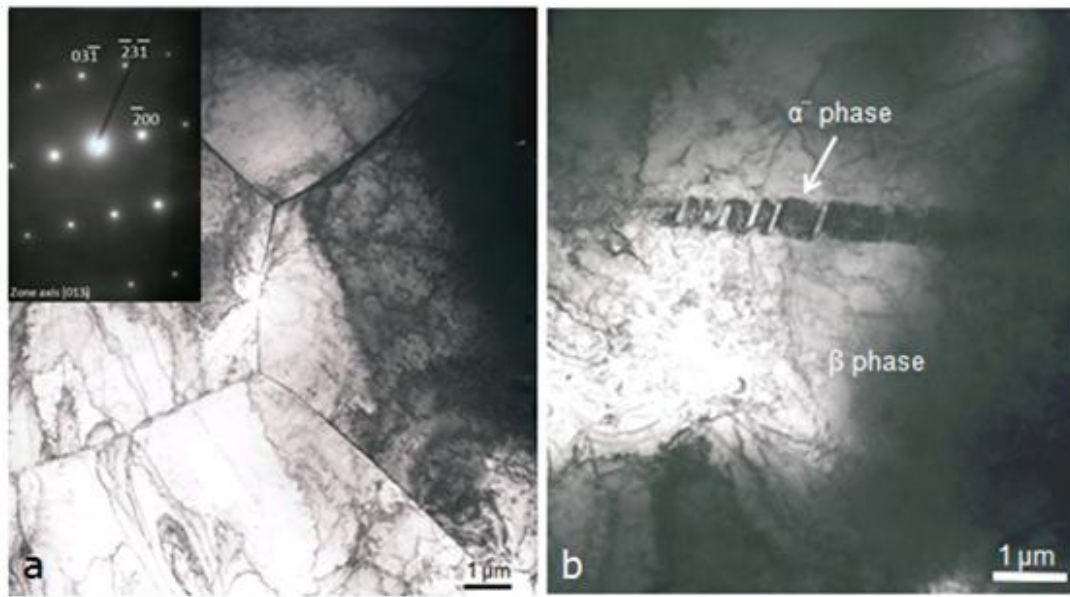


Figure 4

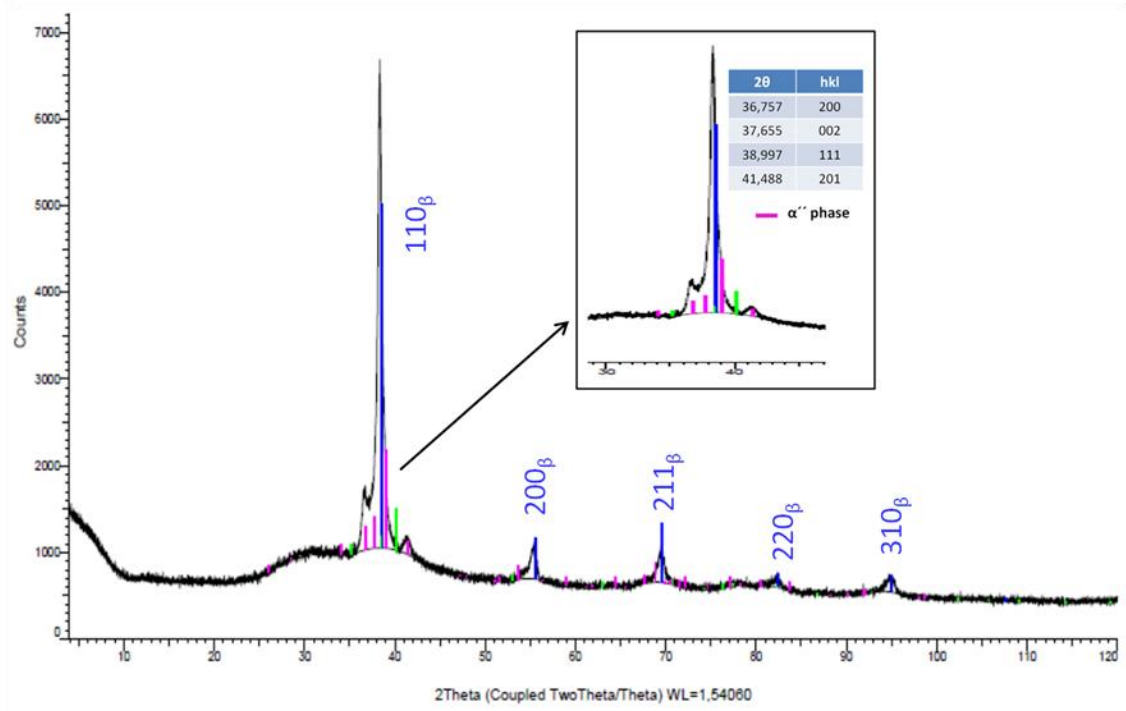


Figure 5

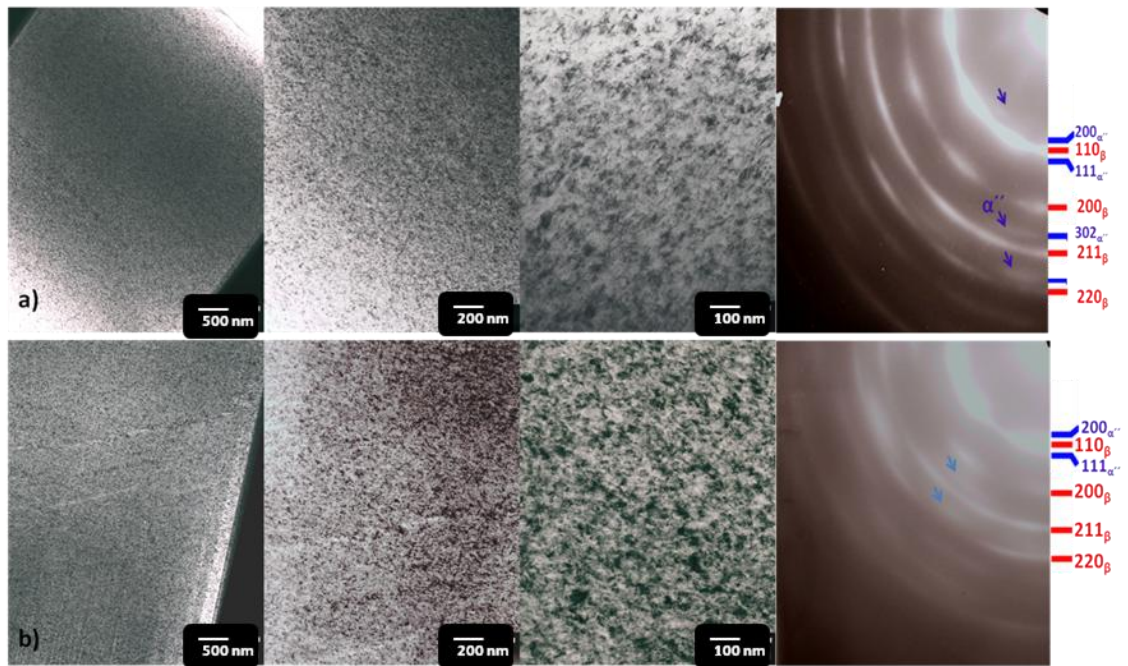


Figure 6

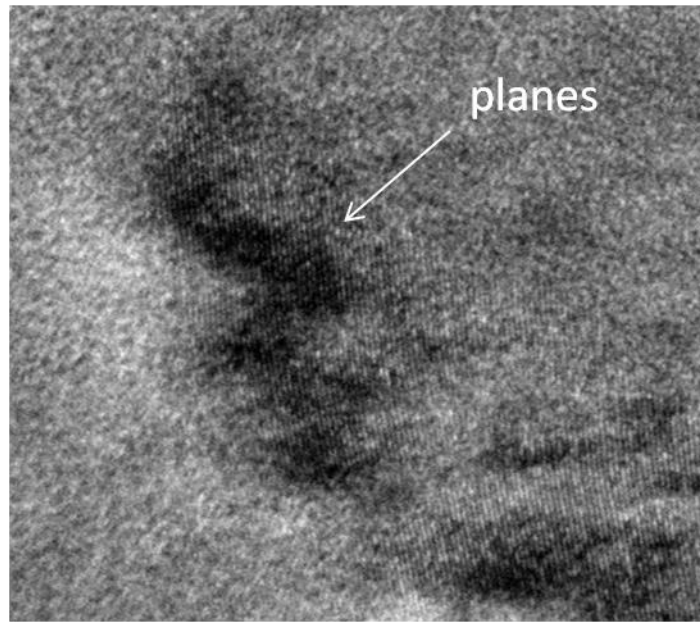


Figure 7

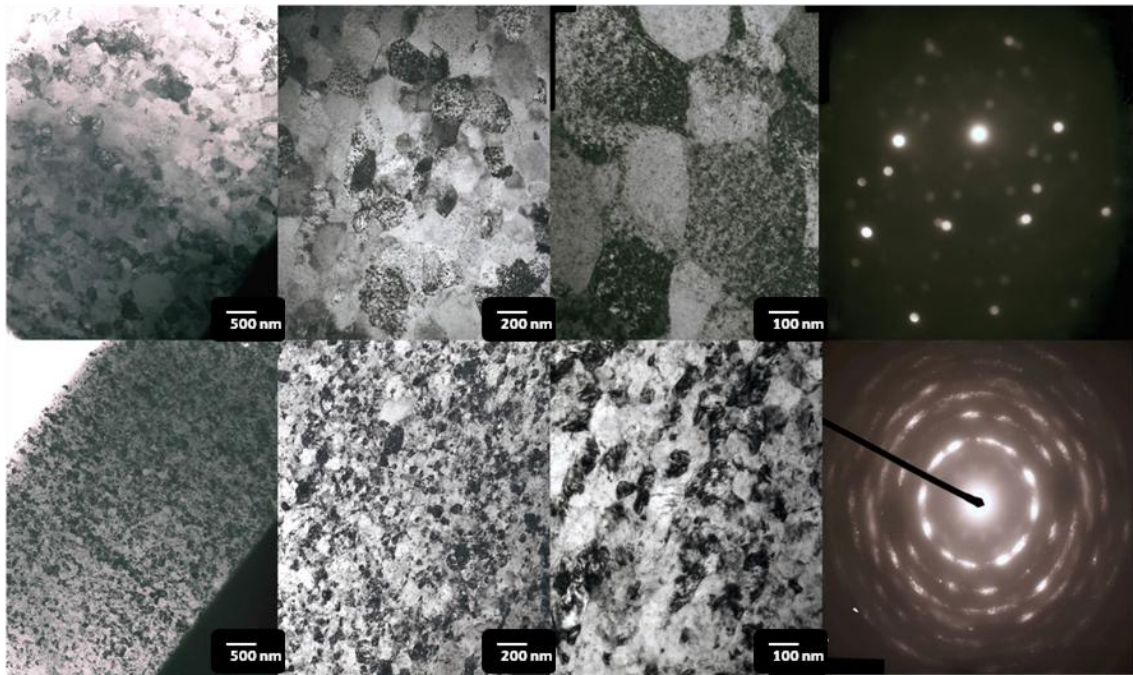


Figure 8

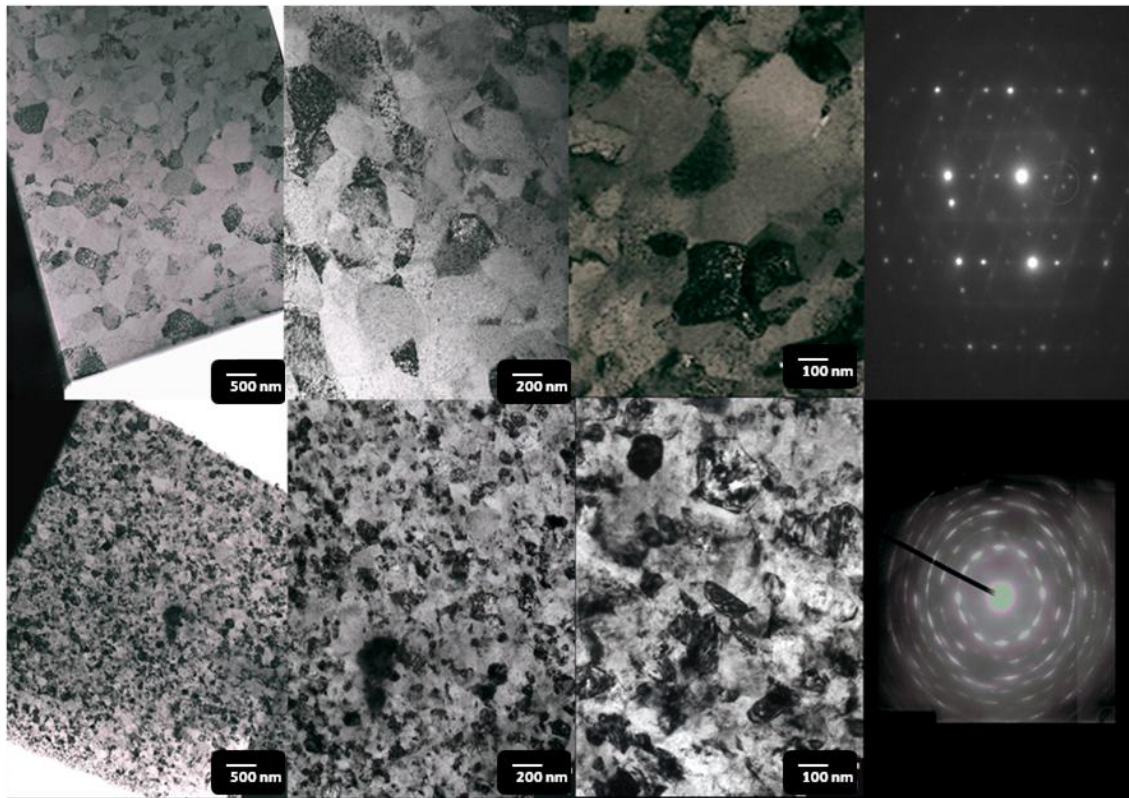


Figure 9

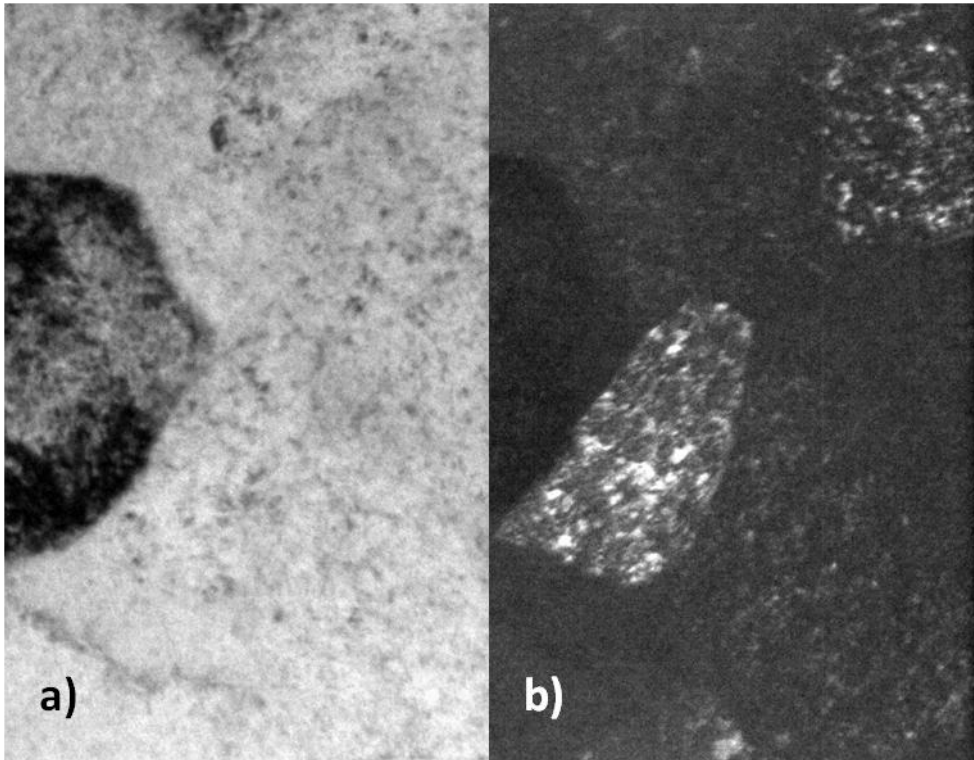


Figure 10

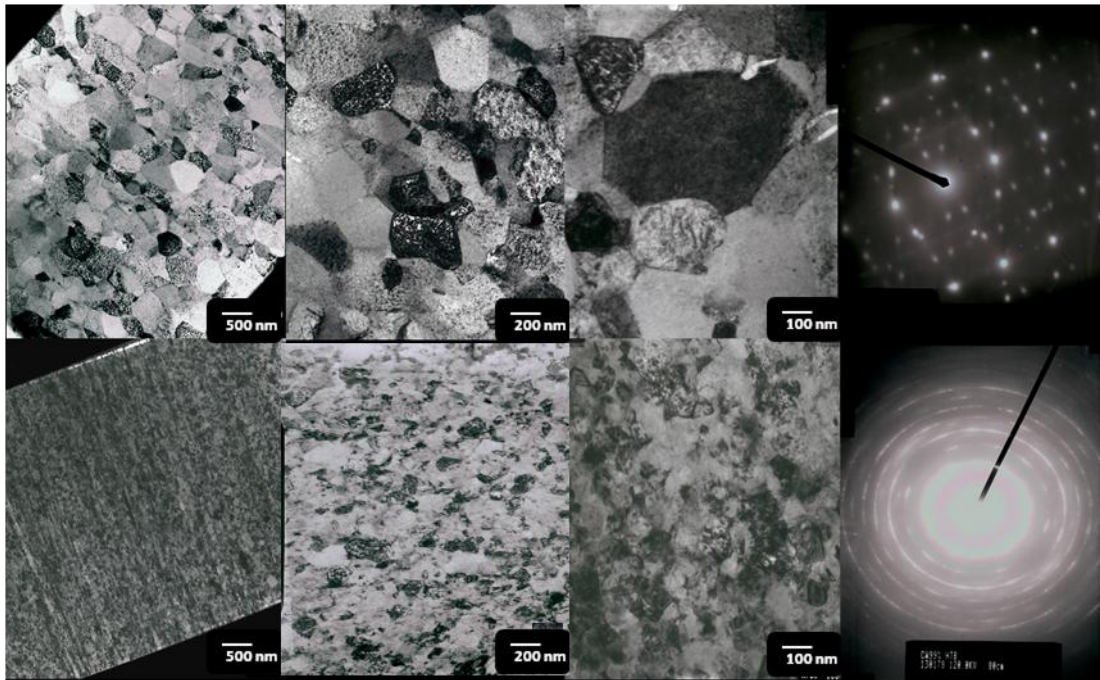


Figure 11

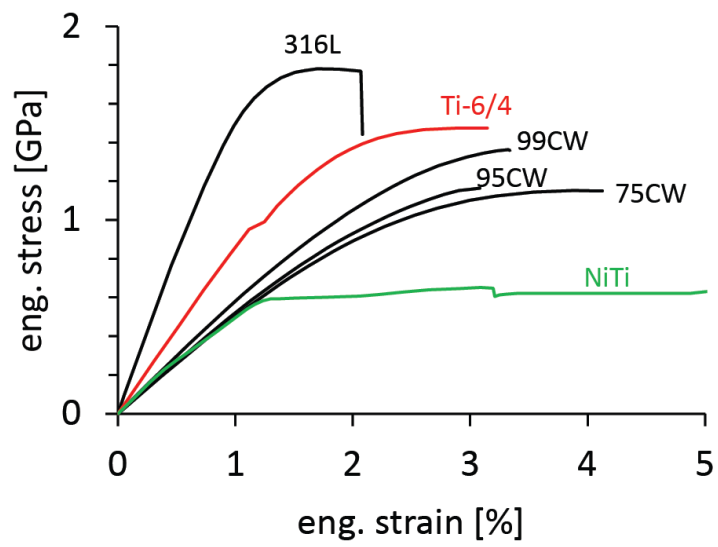
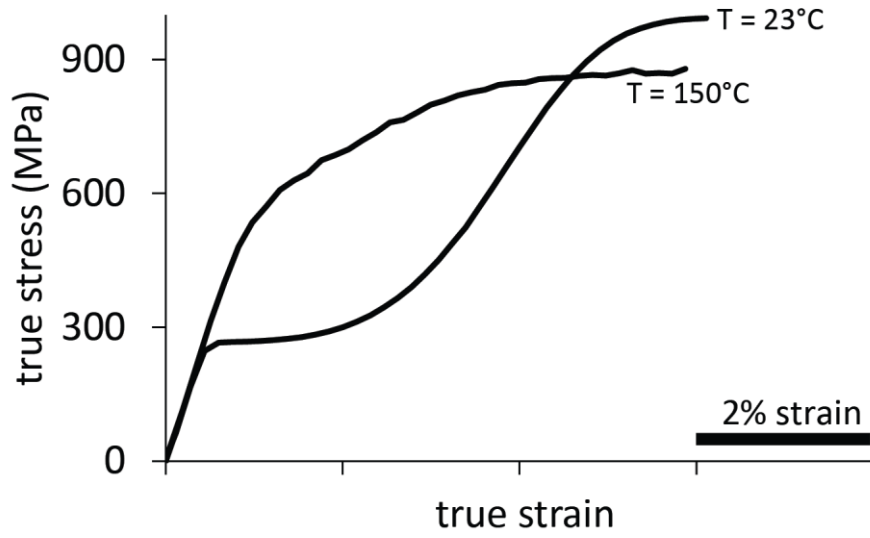


Figure 12

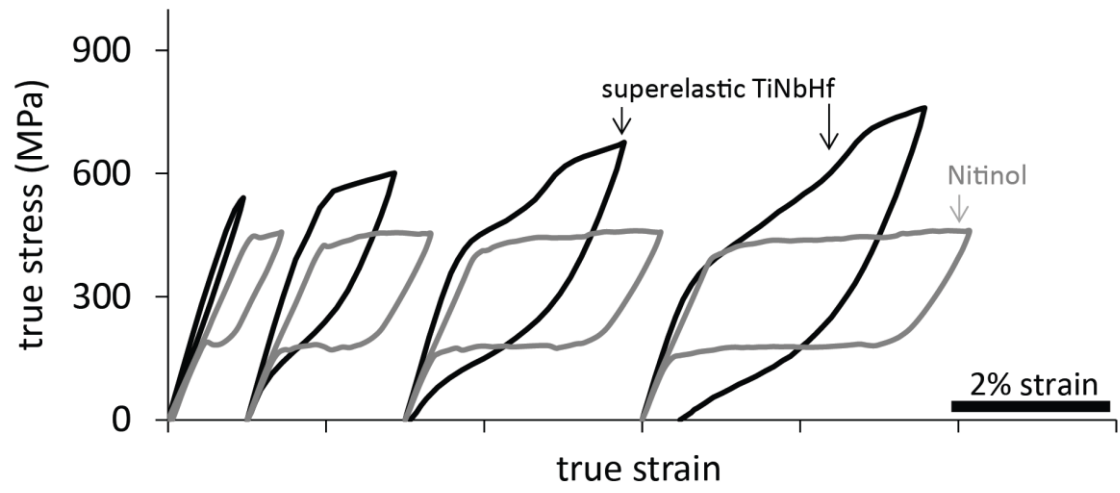
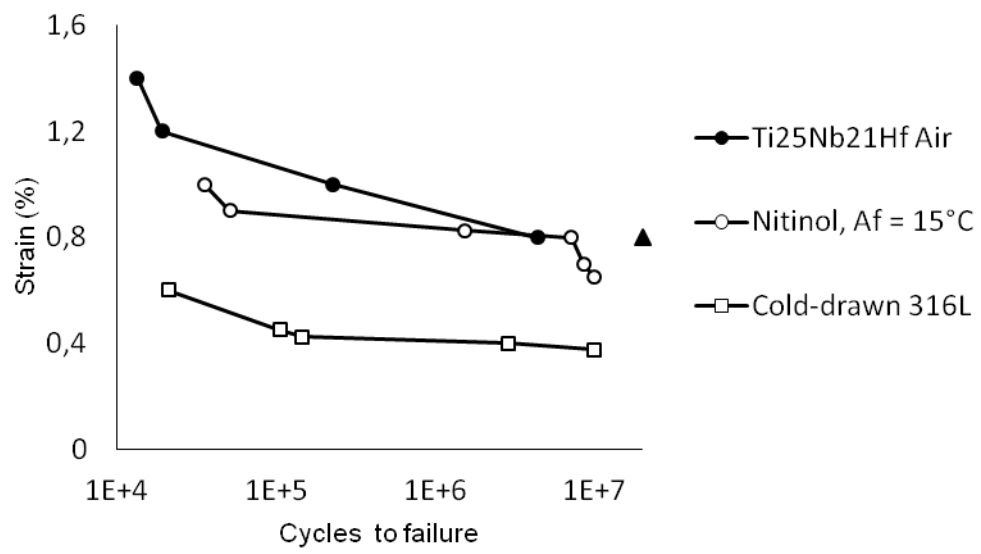


Figure 13



Alloy formulation	% w Element					
	Nb		Hf		Ti	
	Exp.	Theor.	Exp.	Theor.	Exp.	Theor.
<b>Ti-24.8Nb-21Hf</b>	21.41 ±0.65	24.8	21.50 ±0.28	21	57.09 ±0.63	51.2

**Table 1. Values of experimental and theoretical chemical composition for the designed alloy**